Tidal field anisotropy as a tracer of cosmic voids

Sebastian Bustamante $\star^1$, Jaime E. Forero-Romero $\dagger^2$

^{1}*Instituto de Física - FCEN, Universidad de Antioquia, Calle 67 No. 53-108, Medellín, Colombia*
^{2}*Departamento de Física, Universidad de los Andes, Cra. 1 No. 18A-10, Edificio Ip, Bogotá, Colombia*

14 February 2015

ABSTRACT

Finding and characterizing underdense regions (voids) in the large scale structure of the Universe is an important task in cosmological studies. In this paper we present a new algorithm to find voids in cosmological simulations. Our approach is based on algorithms that use the tidal and the velocity shear tensors to locally define the cosmic web. Voids are identified using the fractional anisotropy (FA) computed from the eigenvalues of each web scheme. We define the void boundaries using a watershed transform based on the local minima of the FA and its boundaries as the regions where the FA is maximized. This void identification technique does not have any free parameters and does not make any assumption on the shape or structure of the voids. We test the method on the Bolshoi simulation and report on the density and velocity profiles for the voids found using this new scheme. We find that...

Key words: Cosmology: theory - large-scale structure of Universe - Methods: data analysis - numerical - N-body simulations

1 INTRODUCTION

Voids have been identified as one of the most striking features of the Universe on its larges scales since they were found in the first galaxy surveys (Chincarini & Rood 1975; Gregory & Thompson 1978; Einasto et al. 1980a,b; Kirshner et al. 1981; Zeldovich et al. 1982; Kirshner et al. 1987). However, due to the large volume extension of void regions ($\sim 5 - 10$ Mpch^{-1}), statistically meaningful catalogues of voids (Pan et al. 2012; Sutter et al. 2012; Nadathur & Hotchkiss 2014) have only become available through modern galaxy surveys such as the two-degree field Galaxy Redshift Survey (2dF) (Colless et al. 2001, 2003) and the Sloan Digital Sky Survey (SDSS)(York et al. 2000; Abazajian et al. 2003). These observational breakthughs generated a great interest in the last decade to study voids (Hoyle & Vogeley 2004; Croton & et al. 2004; Rojas et al. 2005; Ceccarelli et al. 2006; Patiri et al. 2006; Tikhonov 2006; Patiri et al. 2006; Tikhonov 2007; von Benda-Beckmann & Müller 2008; Foster & Nelson 2009; Ceccarelli et al. 2013; Sutter et al. 2014).

On the theoretical side the basic framework that explains the origin of voids was established in the seminal work of Zel'dovich (1970) and refined in the following decades. The first detailed theoretical models describing formation, dynamics and properties of voids (Hoffman & Shaham 1982;

Icke 1984; Bertschinger 1985; Blumenthal et al. 1992) were complemented and extended by numerical studies (Martel & Wasserman 1990; Regos & Geller 1991; van de Weygaert & van Kampen 1993; Dubinski et al. 1993; Bond et al. 1996). Currently, the most popular approach to study voids relies on N-body simulations. For an extensive compilation of previous numerical works we refer the reader to Colberg et al. (2008).

The relevance of voids to cosmological studies can be summarized in three aspects (Platen et al. 2007). Firstly, voids are a key ingredient of the Cosmic Web. They dominate the volume distribution at large scales and additionally, compensating overdense structures in the total matter budget. Secondly, voids provide a valuable resource to estimate cosmological parameters as their structure and dynamics are sensitive to them. Finally, they are a largely pristine environment to test galaxy evolution.

Although visual recognition of voids in galaxy surveys and simulations is possible in most cases, we need a clear algorithmic identification procedure to make statistical studies. Nevertheless, the community has not reached yet an unambiguous definition of cosmic voids, with many different void finding techniques in the literature (for a detailed comparison of different schemes, see the publication on the results of the Void Finder Comparison Project Colberg et al. (2008)). In spite of the diversity of existing schemes, they can be roughly classified into two types. First, geometric schemes based on point distributions (either real or redshift space) of galaxies in surveys or dark matter halos in simulations

$\star$ sebastian.bustamante@udea.edu.co
$\dagger$ je.forero@uniandes.edu.co

(Kauffmann & Fairall 1991; Müller et al. 2000; Gottlöber et al. 2003; Hoyle & Vogeley 2004; Brunino et al. 2007; Foster & Nelson 2009; Micheletti & et al. 2014; Sutter et al. 2014). Second, schemes based on the smooth and continuous matter density field either from simulations or from reconstruction procedures on surveys (Plionis & Basilakos 2002; Colberg et al. 2005; Shandarin et al. 2006; Platen et al. 2007; Neyrinck 2008; Muñoz-Cuartas et al. 2011; Neyrinck et al. 2013; Ricciardelli et al. 2013). Our work is based on the second kind of schemes.

Here we introduce a new algorithm to define voids over the continous matter density or velocity distribution defined on a fixed and homogeneous spatial grid. The algorithm is based on two tensorial schemes used to classify the cosmic web. The first (the T-web) is based on the Hessian of the gravitational potential or tidal tensor (Hahn et al. 2007; Forero-Romero et al. 2009). The second (the V-web) is based on the velocity shear tensor (Hoffman et al. 2012). Our procedure allows a description of the internal structure of voids that goes beyond a simple definition of a void as just an underdense regions in the large-scale matter distribution. The tidal and the shear tensors encode more information than the density field as they trace the collapsing or expanding nature of the matter field, which defines the dynamics of the Cosmic Web.

The tracer that we use to define the voids is the fractional anisotropy (FA) computed from the set of eigenvalues of the tensor under consideration. The FA was initially introduced by Basser (1995) to quantify the anisotropy degree of the diffusivity of water molecules through cerebral tissue in nuclear magnetic resonance imaging and Libeskind et al. (2013) introduced this concept in the context of Cosmic Web classification schemes.

Once we establish the FA as a void tracer, we proceed to identify individual voids as basins of FA local minima. At this point we implement a *watershed transform algorithm* (Beucher & Lantuejoul 1979; Beucher & Meyer 1993) which has been used to define voids as catching basins of local minima of the density field (Platen et al. 2007; Neyrinck 2008).

This paper is organized as follows. In Section 2 we describe the algorithms we use to find the cosmic web in N-body simulations. In Section 3 we explain in detail our void finder based on the fractional anisotropy of the tidal and shear tensor fields. In Section 4 we describe the N-body simulation we use to test our algorithm. Our results are presented in 5 to finally comment and conclude about these findings in Section 6.

2   ALGORITHMS TO FIND THE COSMIC WEB

In next two subsections we describe the major features of the two algorithms (T-web and V-web) we use to find and classify the cosmic web in cosmological N-body simulations. These schemes have also been used to develop other kind of studies such as the alignment of the shape, spin and peculiar velocity of dark matter halos with the cosmic web (Libeskind et al. 2013; Forero-Romero et al. 2014). We refer the reader to the paper of Forero-Romero et al. (2009) and Hoffman et al. (2012) to read a detailed description of each algorithm.

2.1   The tidal web (T-Web)

This scheme was initially proposed by Hahn et al. (2007) as an alternative for classifying the Cosmic Web based on the tidal tensor. The tidal tensor allows a classification in terms of the orbital dinamics of the matter field. This approach extends to second-order the equations of motion around local minima of the gravitational potential. The second-order term corresponds to the tidal tensor, which is defined as the Hessian matrix of the normalized gravitational potential.

$$T_{\alpha\beta} = \frac{\partial^2 \phi}{\partial x_\alpha \partial x_\beta}, \tag{1}$$

where the physical gravitational potential has been rescaled by a factor of $4\pi G \bar{\rho}$ in such a way that ϕ satisfies the following Poisson equation

$$\nabla^2 \phi = \delta, \tag{2}$$

with $\bar{\rho}$ the average density in the Universe, G the gravitational constant and δ the dimensionless matter overdensity.

Since the tidal tensor can be represented by a real and symmetric 3×3 matrix, it is always possible to diagonalize it and obtain three real eigenvalues $\lambda_1 \geqslant \lambda_2 \geqslant \lambda_3$ with its corresponding eigenvectors $\mathbf{u}_1$, $\mathbf{u}_2$, $\mathbf{u}_3$. The eigenvalues are indicators of the local orbital stability in each direction $\mathbf{u}_i$. The sign of the eigenvalues can be used to classify the Cosmic Web. The number of positive (stable) or negative (unstable) eigenvalues allows to label a location into one of the next four types of environment: voids (3 negative eigenvalues), sheets (2), filaments (1) and knots (0).

A modification to this scheme was introduced by Forero-Romero et al. (2009) by means of a relaxation of the stability criterion. The relative strength of each eigenvalue is no longer defined by the sign, but instead by a threshold value λ_{th} that can be tuned in such a way that the visual impression of the web-like matter distribution is reproduced.

2.2   The velocity web (V-Web)

We also use a kinematic scheme to define the Cosmic Web environment in the simulation introduced by Hoffman et al. (2012). The V-web scheme for environment finding is based on the local velocity shear tensor calculated from the smoothed dark matter velocity field in the simulation. This tensor is given by the following expression

$$\Sigma_{\alpha\beta} = -\frac{1}{2H_0} \left(\frac{\partial v_\alpha}{\partial x_\beta} + \frac{\partial v_\beta}{\partial x_\alpha} \right), \tag{3}$$

where v_α and x_α represent the α component of the comoving velocity and position, respectively. Like the tidal tensor, $\Sigma_{\alpha\beta}$ can be represented by a 3×3 symmetric matrix with real values, making it possible to find three real eigenvalues and its corresponding eigenvectors.

In this case we also use the relative strength of the three eigenvalues with respect to a threshold value λ_{th} to classify the cosmic web in the four web types already mentioned.

Usually, the threshold is a free parameter that is tuned to reproduce the visual appearence of the comic web. In this paper we take a different approach. We find the optimal
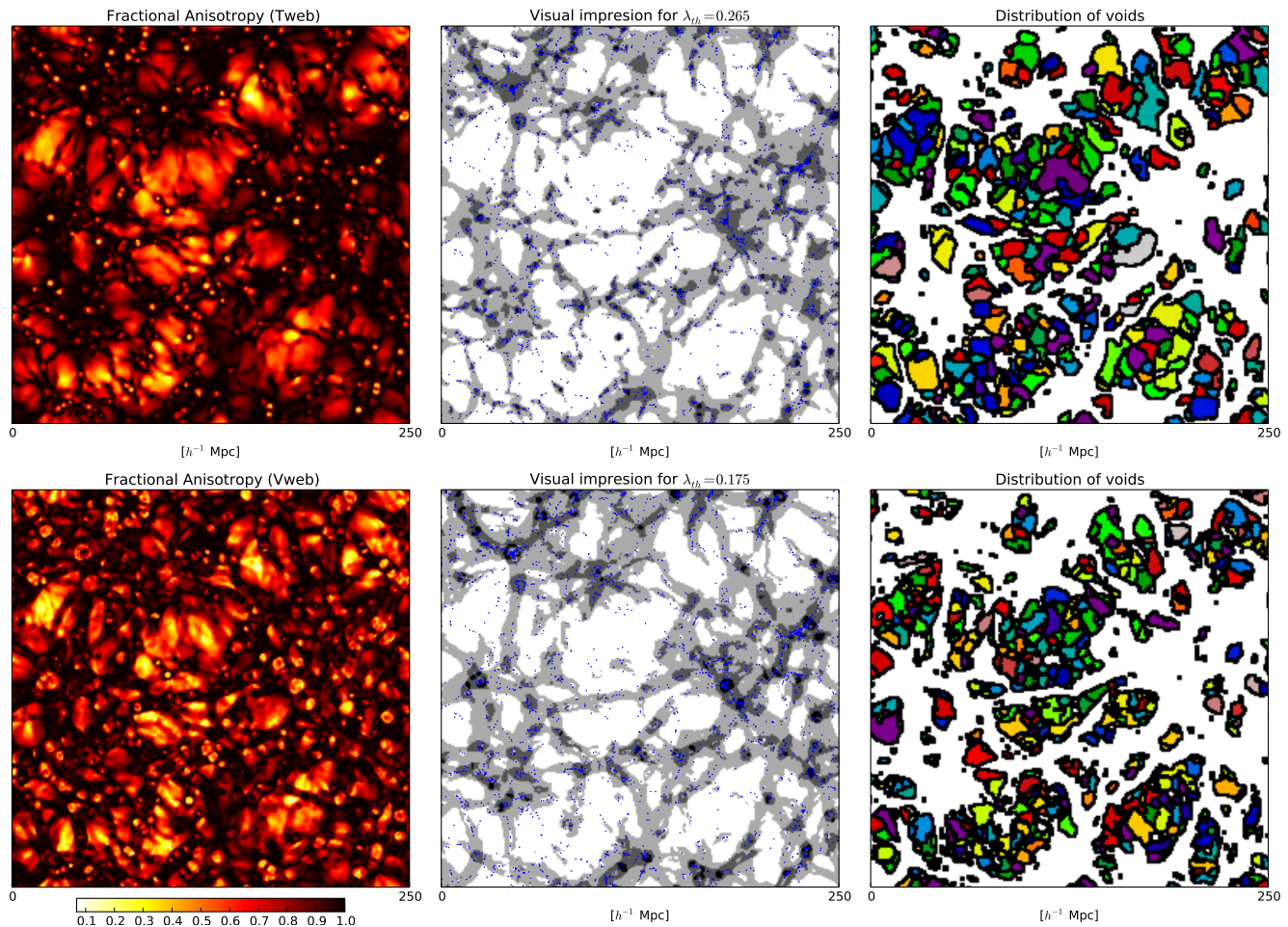
Figure 1. Left colum. Visual impression of the Fractional Anisotropy field over a slide of the simulation for each web scheme (T-Web top. V-Web bottom). Middle column. Cosmic Web identification. Voids are white, sheets are light gray, filaments are dark gray and knots are black. Right column. Colors are voids identified by our Fractional Anisotropy method.

value of the threshold based on the maximization of the fractional anisotropy field in the locations label as filaments and walls. This is described in detailed in the next Section.

3   A NEW VOID FINDING TECHNIQUE

3.1   The fractional anisotropy

The fractional anisotropy (FA), as developed by Basser (1995), was conceived to quantify the anisotropy degree of a diffusion process, e.g. the diffusivity of water molecules through cerebral tissue in nuclear magnetic resonance imaging. Here we present the FA, much in the same way as Libeskind et al. (2013), to use it as a tracer of cosmic voids.

The FA is defined as follows.

$$\text{FA} = \frac{1}{\sqrt{3}} \sqrt{\frac{(\lambda_1 - \lambda_3)^2 + (\lambda_2 - \lambda_3)^2 + (\lambda_1 - \lambda_2)^2}{\lambda_1^2 + \lambda_2^2 + \lambda_3^2}}, \quad (4)$$

where the eigenvalues can be taken from either the T-web or the Vweb (FA-T-web and FA-Vweb respectively). Such as it is defined, FA= 0 corresponds to an isotropic distribution ($\lambda_1 = \lambda_2 = \lambda_3$) and FA= 1 with a highly anisotropic distribution.

In the left and middle panels of Figure 1 we show the FA field and web classification for both web schemes over a slice of an N-body simulation (described in Section 4). Comparing these two panels we see that voids and knots (white and black in the middle panel of Figure 1) display low FA values at their centres, becoming gradually more anisotropic at outer regions. On the other hand the filamentary structure (grey in the middle panel of Figure 1) is traced by high FA values. These characteristics are key to use the FA as a tracer of cosmic voids.

3.2   Fractional anisotropy as a void tracer

Voids are regions where $\lambda_3 \leqslant \lambda_2 \leqslant \lambda_1 \leqslant \lambda_{th}$. This implies that a void is completely fixed by the relative strength of the λ_1 eigenvalue with respect to the threshold. As we increase/decrease the threshold value λ_{th}, voids increase/decrease progressively through contours of increasing/decreasing λ_1. Voids are thus characterized by low values of both FA and λ_1.

In Fig. 2 we show that the these two values are indeed closely correlated. The right panel shows the correlation between λ_1 and δ for all the grid cells in the simulation while
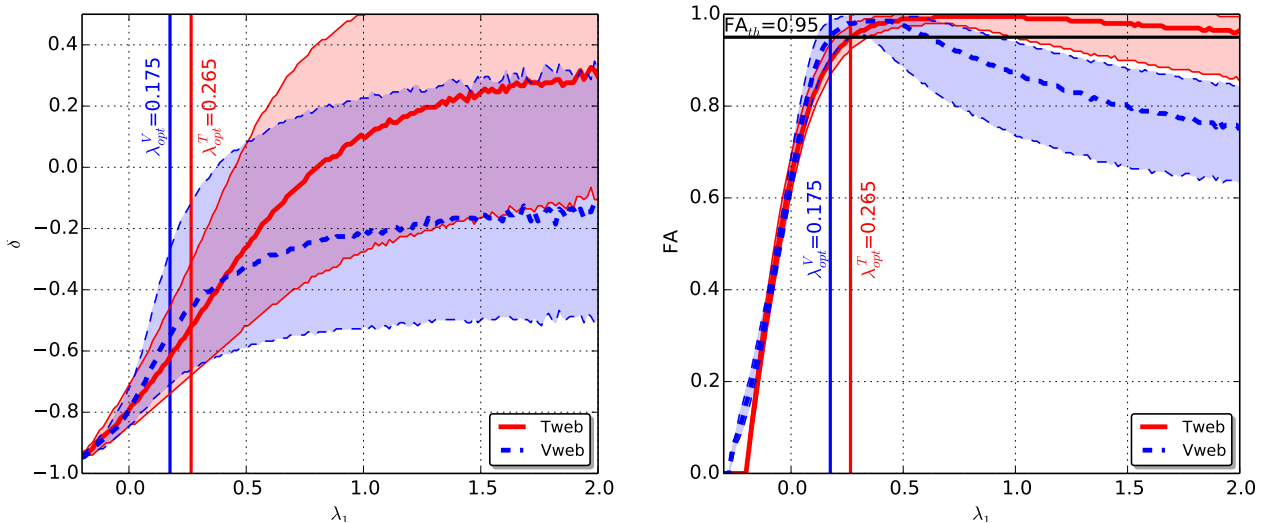
Figure 2. Distributions of the FA (left panel) and the density field (right panel) with respect to the eigenvalue λ_1 for each web scheme (T-web, red lines. Vweb, blue lines) as calculated over all cells of the grid. Thick central lines correspond with the median and filled regions with the 50% of the distribution.

the right panel shows the correlation between λ_1 and the FA. This shows that the overdensity has a large scatter at fixed λ_1.

From Figs. 1 and 2 we conclude that the FA is a good tracer of voids as it is almost perfectly correlated with low values of λ_1. We propose that voids should be composed completely by regions of FA< 0.95. If we increase the values of λ_1 from its minimum until it we reach FA= 0.95 in 2 we find that this correspond to critical values of $\lambda_1^T = 0.265$ and $\lambda_1^V = 0.175$ for the T-web and Vweb, respectively. This means that setting λ_{th} to either λ_1^T/λ_1^V automatically produces voids with all the cells FA< 0.95. The middle panels in Figure 1 show the web classification for this choice of λ_{th}, demonstrating that this FA level is a sensitive choice to define voids.

3.3 Defining voids with a watershed algorithm

The previous section shows that FA is a good void tracer, but it does not automatically suggest how to define the boundary of individual voids. For this purpose, we use the *watershed transform algorithm* (Beucher & Lantuejoul 1979; Beucher & Meyer 1993) to identify a void as the basin of FA local minimum. The advantage of this definition is that it does not require any assumption on the shape and/or morphology of the tentative voids.

However, there are two main differences in our approach with respect to other watershed implementations. First, the watershed technique commonly uses the the density field instead of the FA field as we do in this paper (Platen et al. 2007; Neyrinck 2008). Second, we estimate all relevant quantities on a Cartesian mesh of fixed cell size, while other works use an adaptive Delaunay tessellation (Schaap & van de Weygaert 2000). However, from the analysis of our results it does not introduce supurious results, at least with the mass resolution we have in the N-body simulation.

The watershed algorithm also needs a threshold value to reduce spurious features and prevent void hierarchization.

If the density field is used, a typical threshold is $\delta = -0.8$ (Platen et al. 2007), which means that any ridge between two voids with overdensity below that value is removed to merge the respective voids. In our case we have to find a corresponding FA value to define this threshold.

In Figure 2 we find the correlations of the eigenvalue λ_1 with he matter overdensity (left panel) and the FA (right panel). We can use this information to find the FA threshold. From the left panel we see that an underdensity of $\delta = -0.8$ is correspond to values of $\lambda_1 = 0.0$, regardless of the web-finding scheme. From the second panel we have a very tight correlation of λ_1 with the FA, indicating that in turn $\lambda_1 = 0.0$ corresponds to a FA=0.65 which is the value that we have used to remove ridges.

The right column in Figure 1 shows all the individual voids that have been identified using the watershed algorithm on the FA field. In what follows we describe the numerical simulation we have used to find voids and their detailed properties characterization.

4 NUMERICAL SIMULATION

We use the Bolshoi simulation to test our void finding method. This simulation follows the non-linear evolution of a dark matter density field on a cubic volume of size $250h^{-1}$Mpc sampled with 2048^3 particles. The cosmological parameters in the simulation are $\Omega_{\rm m} = 0.27$, $\Omega_\Lambda = 0.73$, $h = 0.70$, $n = 0.95$ and $\sigma_8 = 0.82$ for the matter density, cosmological constant, dimensionless Hubble parameter, spectral index of primordial density perturbations and normalization for the power spectrum, respectively. These values are consistent with the ninth year of data of the Wilkinson Microwave Anisotropy Probe (WMAP) (Hinshaw et al. 2013). For more detailed technical information about the simulation, see Klypin et al. (2011).

We use data for the cosmic web identification that is publicly available through the MultiDark database `http://www.multidark.org/MultiDark/` which is described in

Riebe et al. (2013). Here we briefly describe the process to obtain the data. For details see Forero-Romero et al. (2009) (T-Web) and Hoffman et al. (2012); Forero-Romero et al. (2014) (V-Web). This data is based on a *cloud-in-cell* (CIC) interpolation of the density and velocity fields of the simulation onto a grid of 256^3 cells, corresponding to a spatial resolution of $0.98h^{-1}$Mpc per cell side. These fields are smoothed with a gaussian filter with a width of $\sigma = 0.98h^{-1}$Mpc. The tidal and shear tensors and corresponding eigenvalues are computed through finite-differences over the potential and velocity fields.

5 RESULTS

We limit our results to voids with effective radius larger than the smoothing length of the density field, i.e. $\sim 1h^{-1}$Mpc. Below that scale numerical resolution effects become important. With that choice we find a volume filling fraction 54.88% and 47.06% for the FA-Vweb.

In the following subsections we describe the results for the size distribution and different radial profiles for all our samples.

5.1 The void size distribution

Void shapes exhibit a wide range of geometries. To define their size we use its equivalent spherical radius or effective radius, defined as $r_{\rm eff} = [3/(4\pi)V]^{1/3}$, with V the total volume of the void computed from the individual grid cells assigned to the void. In Figure 3 we show the void size distributions for the T-Web and the V-Web.

We see that the void distribution for the T-Web is broadly consistent with the expectations from a two-barrier problem (Sheth & van de Weygaert 2004). The formation of large voids is limited by the *void-in-void* problem (first barrier), where large voids are constituted hierarchically of smaller ones. In turn, the formation of small voids is damped by the *void-in-cloud* problem (second barrier), where nearby collapsing structures limit the abundance of small embedded voids.

We also find that the V-Web scheme produces an overabundance of small voids compared to the resuls of the T-Web. A large number of these small voids are embedded in overdense regions. They are visible in the middle panel of Figure 1 as small bubbles located inside sheets. The existence of these small voids can be explained by dynamics of shell crossing in collapsing sheets. As matter colides into a sheet, in their symmetry plane one will find crossing ahseets that effectively give a positive divergence in the velocity field, resulting in a void identification by the V-Web algorithm. This points has been discussed in Hoffman et al. (2012).

Comparing the abundance of large voids in the two web schemes, we find that the V-Web is limited to have voids on the scale of $\sim 10h^{-1}$Mpc, while the T-Web scheme includes voids as large as $\sim 15h^{-1}$Mpc. Large voids in the T-Web scheme have a velocity structure that induces a split by the watershed algorithm in the V-Web. This is evident in the right panel of Figure 1.

5.2 Subcompensated and overcompensated voids

We find that voids are distributed in two different families differentiated by the presence/absence of an overdense matter ridge in their density profiles. To discriminate each void in one of the families we use the compensation index $\mathcal{C}$. It is defined as the mass of a void enclosed in a spherical volume of radius R and normalized by the mass of the same volume assuming it is filled by matter with the mean background density.

$$\mathcal{C} = \frac{M_v}{\overline{M}} = \frac{3}{2R^3} \int_0^R [\delta(r) + 1]r^2 dr \qquad (5)$$

We choose an integration radius of $R = 4r_{\rm eff}$, that is large enough to enclose the compensation ridge for a typical void in case there is one. This leads us to voids with $\mathcal{C} > 1$ having more mass than expected, constituting the family of overcompensated voids. These voids generally exhibit a compensation ridge associated to dense nearby structures. In the same fashion, voids with $\mathcal{C} < 1$ constitute the family of subcompensated voids.

In Figure 4 we show the density and velocity profiles of voids splitted in these two families. In the left column it becomes clear the difference between sub- and overcompensated voids.

5.3 Density profiles

We calculate the contrast density, radial-projected velocity and FA profiles. For this purpose we catalogue all the voids in several radial bins in order to capture possible size effects; moreover we show profiles for both, subcompensated and overcompensated voids. Then, for each void, we take the distance of each member cell to the void centre along with the properties of interest. Normalizing these distances with the effective radius, we stack all the voids of a radial bin in order to compute the radial profiles.

Figure 4 shows the results of stacked density profiles for different void sizes. We normalize the radial coordinate with the effective radius to check for possible universal features among voids. We calculate the profile out to a radius 8 $r_{\rm eff}$ to capture the the point where the overdensity reaches the mean value.

A first interesting result is the overdensity value at the void's center. We find that larger voids have a lower overdensity value. The largest voids ($8.3 - 12\ h^{-1}$Mpc) have an underdensity ≈ -0.95 while smaller voids ($2 - 3.2\ h^{-1}$Mpc) fall around $\delta \approx -0.8$ at their centers. This holds for both web schemes.

These values are consistent with most of the void finding schemes based on smooth and continuous fields from simulation or reconstruction procedures on surveys (Plionis & Basilakos 2002; Colberg et al. 2005; Shandarin et al. 2006; Platen et al. 2007; Neyrinck 2008; Muñoz-Cuartas et al. 2011; Neyrinck et al. 2013; Ricciardelli et al. 2013), unlike geometrical approaches based on point distributions, where central density values are generally higher (Colberg et al. 2008).

A second feature about these profiles is their steepnes at inner regions. In subcompensated voids, larger voids are steeper. Smaller voids exhibit moderate slopes, reaching the
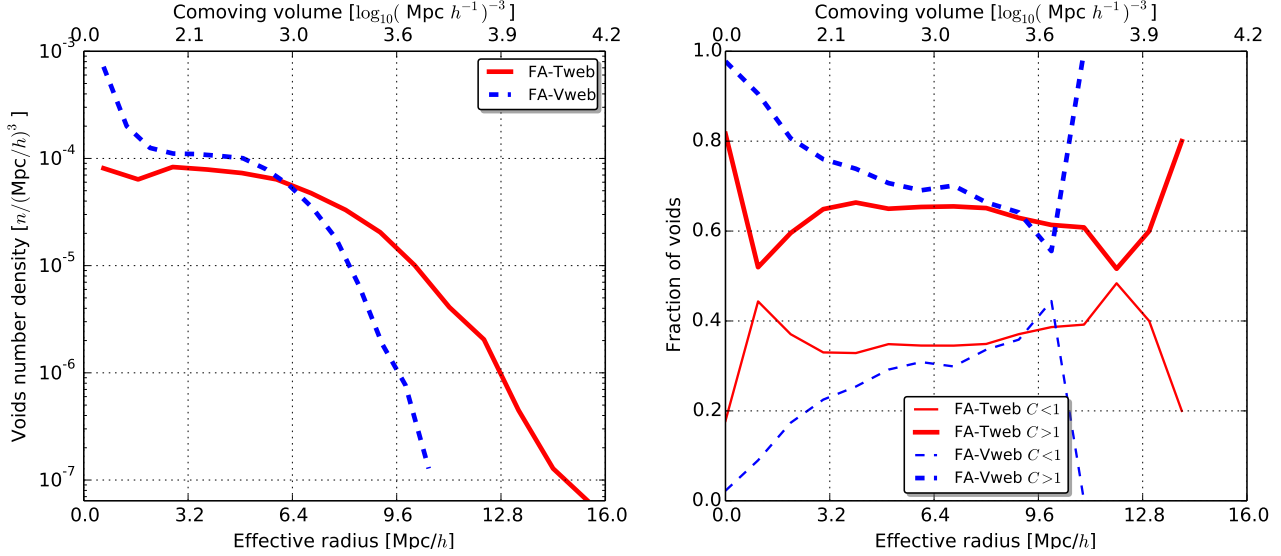
Figure 3. Volume size distribution of voids for both catalogues. FA-T-web (continuous red curves), FA-Vweb (dashed blue curves). Left panel, total distributions. Right panel, distributions of subcompensanted and overcompensanted voids.

mean density at larger radii than larger voids. This suggests that smaller subcompensated voids are embedded into low density structures like voids or walls, while arge subcompensated voids are surrounded by dense structures, reaching the mean density at lower effective radii than smaller voids. In overcompensated voids larger voids reach first both the compensation ridge and then the mean density value.

Regarding overcompensated voids, a final result is related to the height of the compensation ridge: the larger the void size, the lower the ridge height. This implies that overcompensated smaller voids are embedded in very high density regions, unlike their subcompensated counterpart, thus indicating two possibly different processes for small voids formation. Larger voids exhibit lower ridges as outer radial layers also includes all sort of structures, thus being the difference between large overcompensated and subcompensated voids less conclusive.

All the previous results hold for both finding schemes. This suggests an universal behaviour for the radial density profile in two families of subcompensated and overcompensated voids. This goes in the same direction of recent results about the internal (Colberg et al. 2005; Ricciardelli et al. 2013) and external structure of voids (Lavaux & Wandelt 2012; Hamaus et al. 2014). Our results extend the findings of Hamaus et al. (2014) into the range of voids with size $r_{\rm eff} < 10h^{-1}{\rm Mpc}$.

5.4   Velocity profiles

In Figure 5 we present the radial velocity profiles. Positive values correspond to outflows with respect to the center.

We find that subcompensated voids have outflowing velocity profiles all the way up to the effective radius where the average radial density reaches the average value. For voids with sizes $r_{\rm eff} < 8h^{-1}{\rm Mpc}$ the outflow is always positive, consistent with the fact that their density profiles do not reach the level $\delta = 0$ in the range of explored radii. This

behaviour indicates that matter is being pulled out of the void into external higher density features.

On the other hand, overcompensated voids initially exhibit and outward profiles, (as expected from a low density region) and approximately at the radius of the compensation ridge, the velocity reaches a peak, decreases and becomes negative, showing the infalling flow of matter further than the compensation ridge. This shows that the high density structures associated to the compensation ridge dominate the matter flow both from inside and outside the void.

As in the density these results also consistent with a Universial velocity profile for voids (Hamaus et al. 2014).

5.5   Fractional Anisotropy profiles

Figure 6 shows the results for the FA profiles. We find that the FA clearly magnifies the difference between the internal profile $r_{\rm eff} < 1$ and the external profile $r_{\rm eff} > 1$. Subcompensated voids in the T-Web reach an asymptotic background value of F=0.8 almost right at $r_{\rm eff} = 2$. For the V-Web the results are similar, albeit rather slowly with the effective radius. Overcompensated voids reach a maximum FA at the same effective radiuus $r_{\rm eff} = 1$ and decline to reach an asymptotic value of FA=0.85 at larger radii.

The central FA values also show a magnified trend with the void size. Larger voids have lower FA values, more clearly than the same trend observed with the central density value. The voids in the V-Web scheme span a larger range of central FA values than in the T-Web scheme.

The difference between the radius where the density ridge is reached ($r_{\rm eff} = 3$) and the radius of the FA ridge ($r_{\rm eff} = 1$) justifies in a more quantiative way the qualitative argument we present in Section 3.3 to define void boundaries in our method. Namely that as we increase the void boundary, we reach first middle density walls, before reashing high density structures associated with high anisotropy, making the FA ridge a natural voids boundary instead of the density ridge.
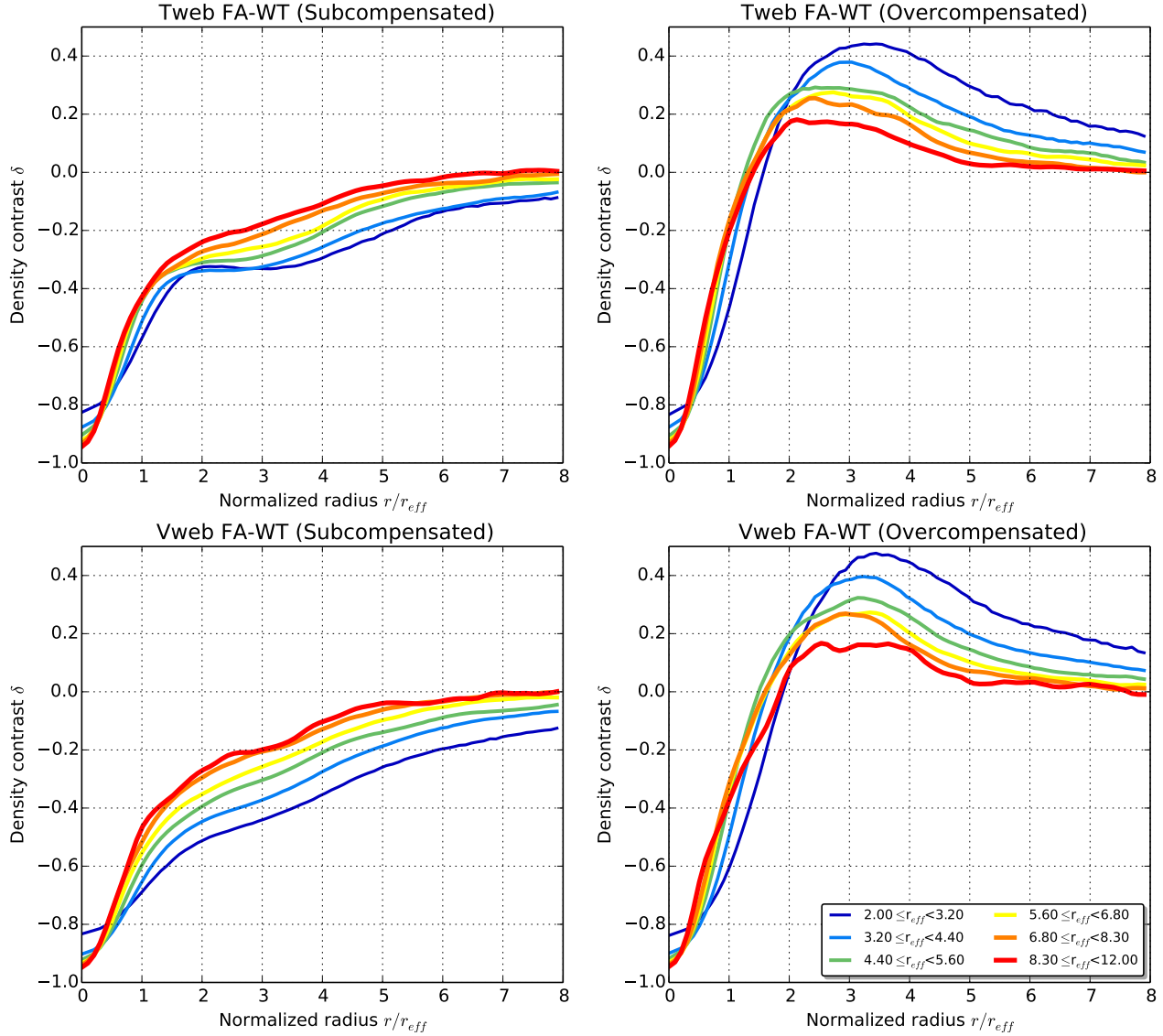
Figure 4. Spherically averaged radial density profile for voids. The sample is split into subcompensated and overcompensated voids (right and left) for the web schemes T-Web and V-Web (top and bottom).

We recognize that our choice produces smaller voids as compared with other voids finding methods, however this has the advantange of voiding the contamination from external structures.

6 CONCLUSIONS

We propose in this paper a new method to find and describe void in cosmological dark matter simulations. The basis of our metho is the anisotropy of the eigenvalues from tensors constructed to describe the cosmic web.

REFERENCES

Abazajian K., et al. (the SDSS Collaboration) 2003, AJ, 126, 2081
Basser P., 1995, NMR in Biomedical Imaging, 8, 333
Bertschinger E., 1985, ApJS, 58, 1
Beucher S., Lantuejoul C., 1979, in Proceedings International Workshop on Image Processing, CCETT/IRISA, Rennes, France
Beucher S., Meyer F., 1993, Mathematical Morphology in Image Processing. Marcel Deker, New York
Blumenthal G. R., da Costa L. N., Goldwirth D. S., Lecar M., Piran T., 1992, ApJ, 388, 234
Bond J. R., Kofman L., Pogosyan D., 1996, Nature, 380, 603
Brunino R., Trujillo I., Pearce F. R., Thomas P. A., 2007, MNRAS, 375, 184
Ceccarelli L., Padilla N. D., Valotto C., Lambas D. G., 2006, MNRAS, 373, 1440
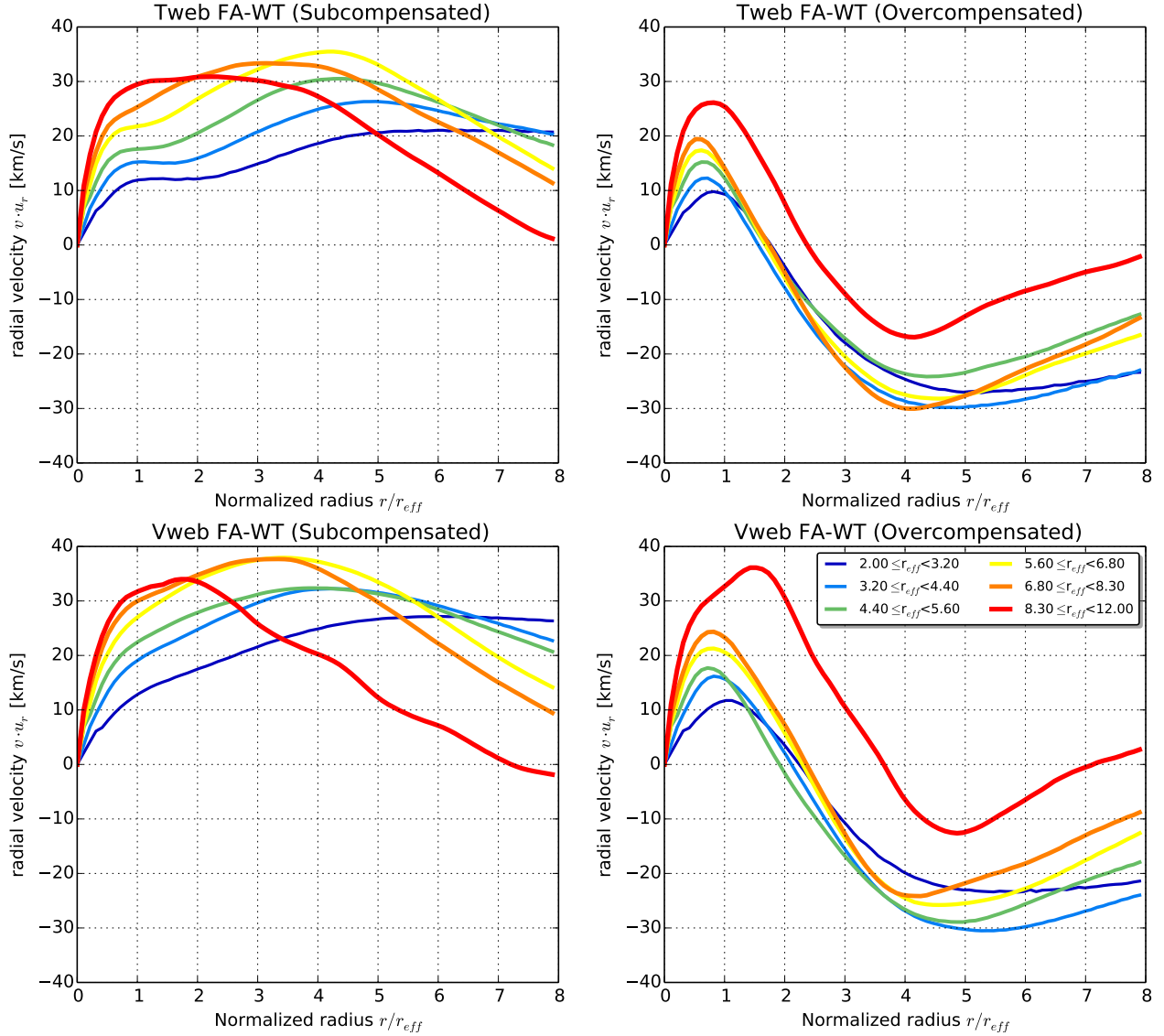Ceccarelli L., Paz D., Lares M., Padilla N., Lambas D. G., 2013, MNRAS, 434, 1435

Figure 5. Spherically averaged radial velocity profile for voids. The sample is split into subcompensated and overcompensated voids (right and left) for the web schemes T-Web and V-Web (top and bottom).

Chincarini G., Rood H. J., 1975, Nature, 257, 294

Colberg J. M., Pearce F., et al. 2008, MNRAS, 387, 933

Colberg J. M., Sheth R. K., Diaferio A., Gao L., Yoshida N., 2005, MNRAS, 360, 216

Colless M., et al. (the 2dFGRS Team), 2001, MNRAS, 328, 1039

Colless M., et al. (the 2dFGRS Team), 2003, VizieR Online Data Catalog, 7226

Croton D. J., et al. 2004, MNRAS, 352, 828

Dubinski J., da Costa L. N., Goldwirth D. S., Lecar M., Piran T., 1993, ApJ, 410, 458

Einasto J., Joeveer M., Saar E., 1980a, MNRAS, 193, 353

Einasto J., Joeveer M., Saar E., 1980b, Nature, 283, 47

Forero-Romero J. E., Contreras S., Padilla N., 2014, MN-RAS, 443, 1090

Forero-Romero J. E., Hoffman Y., Gottlöber S., Klypin A., Yepes G., 2009, MNRAS, 396, 1815

Foster C., Nelson L. A., 2009, ApJ, 699, 1252

Gottlöber S., Łokas E. L., Klypin A., Hoffman Y., 2003, MNRAS, 344, 715

Gregory S. A., Thompson L. A., 1978, ApJ, 222, 784

Hahn O., Porciani C., Carollo C. M., Dekel A., 2007, MN-RAS, 375, 489

Hamaus N., Sutter P. M., Wandelt B. D., 2014, ArXiv e-prints

Hinshaw G. et al., 2013, ApJS, 208, 19

Hoffman Y., Metuki O., Yepes G., Gottlöber S., Forero-Romero J. E., Libeskind N. I., Knebe A., 2012, MNRAS, 425, 2049

Hoffman Y., Shaham J., 1982, ApJL, 262, L23

Hoyle F., Vogeley M. S., 2004, ApJ, 607, 751

Icke V., 1984, MNRAS, 206, 1P

Kauffmann G., Fairall A. P., 1991, MNRAS, 248, 313

Kirshner R. P., Oemler Jr. A., Schechter P. L., Shectman S. A., 1981, ApJL, 248, L57

Kirshner R. P., Oemler Jr. A., Schechter P. L., Shectman
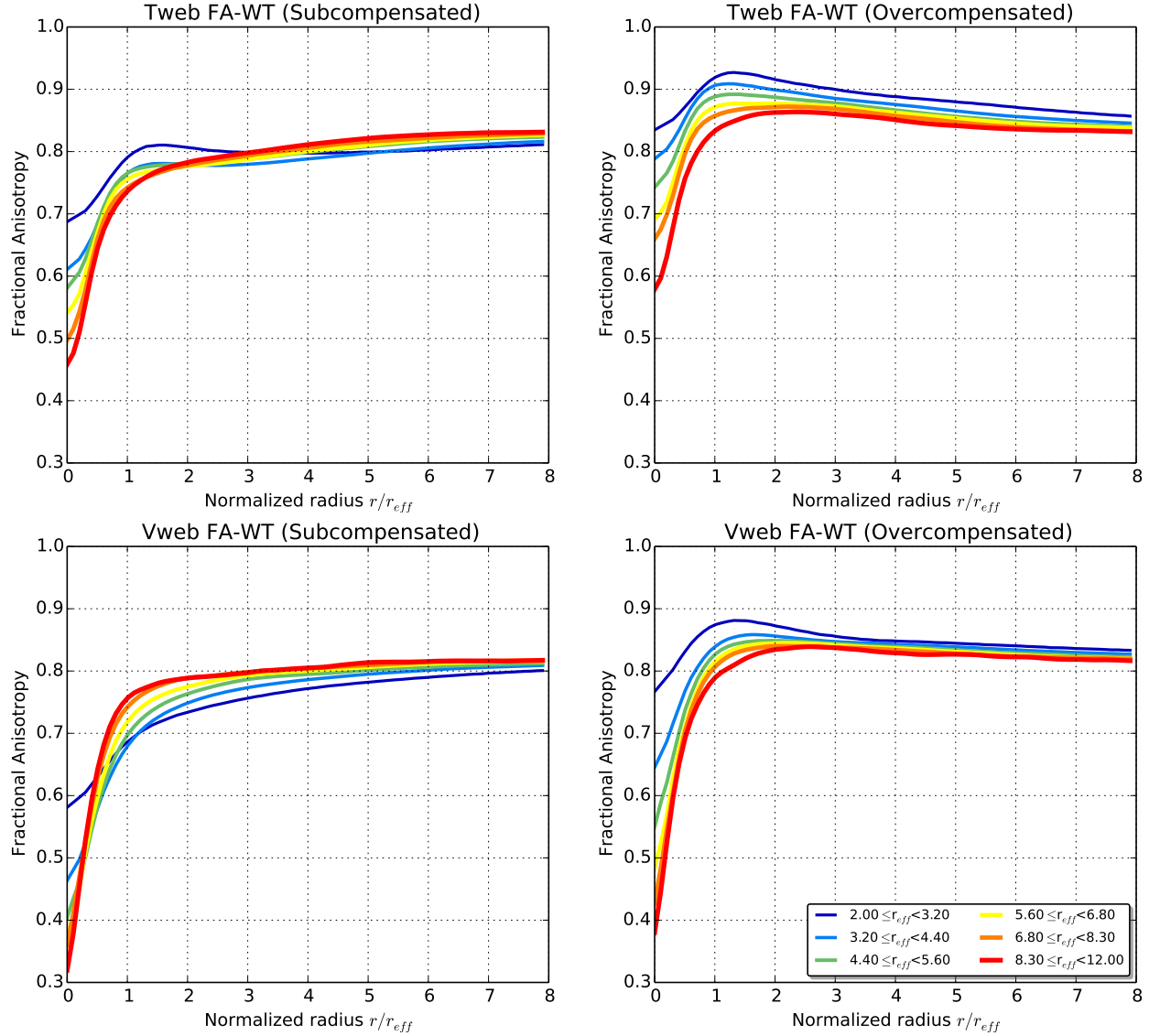
Figure 6. Spherically averaged Fractional Anisotropy profile for voids. The sample is split into subcompensated and overcompensated voids (right and left) for the web schemes T-Web and V-Web (top and bottom).

S. A., 1987, ApJ, 314, 493

Klypin A. A., Trujillo-Gomez S., Primack J., 2011, ApJ, 740, 102

Lavaux G., Wandelt B. D., 2012, ApJ, 754, 109

Libeskind N. I., Hoffman Y., Forero-Romero J., Gottlöber S., Knebe A., Steinmetz M., Klypin A., 2013, MNRAS, 428, 2489

Martel H., Wasserman I., 1990, ApJ, 348, 1

Micheletti D., et al. 2014, ArXiv e-prints

Muñoz-Cuartas J. C., Müller V., Forero-Romero J. E., 2011, MNRAS, 417, 1303

Müller V., Arbabi-Bidgoli S., Einasto J., Tucker D., 2000, MNRAS, 318, 280

Nadathur S., Hotchkiss S., 2014, MNRAS, 440, 1248

Neyrinck M. C., 2008, MNRAS, 386, 2101

Neyrinck M. C., Falck B. L., Szalay A. S., 2013, ArXiv e-prints

Pan D. C., Vogeley M. S., Hoyle F., Choi Y.-Y., Park C.,

2012, MNRAS, 421, 926

Patiri S. G., Betancort-Rijo J., Prada F., 2006, MNRAS, 368, 1132

Patiri S. G., Prada F., Holtzman J., Klypin A., Betancort-Rijo J., 2006, MNRAS, 372, 1710

Platen E., van de Weygaert R., Jones B. J. T., 2007, MNRAS, 380, 551

Plionis M., Basilakos S., 2002, MNRAS, 330, 399

Regos E., Geller M. J., 1991, ApJ, 377, 14

Ricciardelli E., Quilis V., Planelles S., 2013, MNRAS, 434, 1192

Riebe K. et al., 2013, Astronomische Nachrichten, 334, 691

Rojas R. R., Vogeley M. S., Hoyle F., Brinkmann J., 2005, ApJ, 624, 571

Schaap W. E., van de Weygaert R., 2000, A&A, 363, L29

Shandarin S., Feldman H. A., Heitmann K., Habib S., 2006, MNRAS, 367, 1629

Sheth R. K., van de Weygaert R., 2004, MNRAS, 350, 517

Sutter P. M. et al., 2014, ArXiv e-prints

Sutter P. M., Lavaux G., Wandelt B. D., Weinberg D. H., 2012, ApJ, 761, 44

Sutter P. M., Lavaux G., Wandelt B. D., Weinberg D. H., Warren M. S., 2014, MNRAS, 438, 3177

Tikhonov A. V., 2006, Astronomy Letters, 32, 727

Tikhonov A. V., 2007, Astronomy Letters, 33, 499

van de Weygaert R., van Kampen E., 1993, MNRAS, 263, 481

von Benda-Beckmann A. M., Müller V., 2008, MNRAS, 384, 1189

York D. G., et al. (the SDSS Collaboration), 2000, AJ, 120, 1579

Zeldovich I. B., Einasto J., Shandarin S. F., 1982, Nature, 300, 407

Zel'dovich Y. B., 1970, A&A, 5, 84